

Multiwavelength observation of an active M-dwarf star EV Lac and its stellar flare accompanied by a delayed prominence eruption

Shun Inoue^{1*}, Teruaki Enoto^{1,2}, Kosuke Namekata³, Yuta Notsu^{4,5}, Satoshi Honda⁶, Hiroyuki Maehara⁷, Jiale Zhang⁸, Hong-Peng Lu⁸, Hiroyuki Uchida¹, Takeshi Go Tsuru¹, Daisaku Nogami^{9,10} and Kazunari Shibata^{11,12}

¹Department of Physics, Kyoto University, Kitashirakawa-Oiwake-cho, Sakyo-ku, Kyoto, 606-8502, Japan

²RIKEN Cluster for Pioneering Research, 2-1 Hirosawa, Wako, Saitama, 351-0198, Japan

³ALMA Project, NAOJ, NINS, Osawa, Mitaka, Tokyo, 181-8588, Japan

⁴Laboratory for Atmospheric and Space Physics, University of Colorado Boulder, 3665 Discovery Drive, Boulder, CO 80303, USA

⁵National Solar Observatory, 3665 Discovery Drive, Boulder, CO 80303, USA

⁶Nishi-Harima Astronomical Observatory, Center for Astronomy, University of Hyogo, Sayo, Hyogo, 679-5313, Japan

⁷Okayama Branch Office, Subaru Telescope, NAOJ, NINS, Kamogata, Asakuchi, Okayama, 719-0232, Japan

⁸School of Earth and Space Sciences, Peking University, Beijing 100871, China

⁹Department of Astronomy, Kyoto University, Kitashirakawa-Oiwake-cho, Sakyo-ku, Kyoto, 606-8502, Japan

¹⁰Astronomical Observatory, Kyoto University, Sakyo-ku, Kyoto, 606-8502, Japan

¹¹Kwasan Observatory, Kyoto University, Yamashina, Kyoto, 607-8471, Japan

¹²School of Science and Engineering, Doshisha University, Kyotanabe, Kyoto, 610-0321, Japan

*E-mail: inoue.shun.57c@kyoto-u.jp

Received (reception date); Accepted (acceptation date)

Abstract

We conducted 4-night multiwavelength observations of an active M-dwarf star EV Lac on 2022 October 24–27 with simultaneous coverage of soft X-rays (NICER; 0.2–12 keV, Swift XRT; 0.2–10 keV), near-ultraviolet (Swift UVOT/UVW2; 1600–3500 Å), optical photometry (TESS; 6000–10000 Å), and optical spectroscopy (Nayuta/MALLS; 6350–6800 Å). During the campaign, we detected a flare starting at 12:28 UTC on October 25 with its white-light bolometric energy of 3.4×10^{32} erg. At about 1 hour after this flare peak, our H α spectrum showed a blue-shifted excess component at its corresponding velocity of $\sim 100 \text{ km s}^{-1}$. This may indicate that the prominence erupted with a 1-hour delay of the flare peak. Furthermore, the simultaneous 20-second cadence near-ultraviolet and white-light curves show gradual and rapid brightening behaviors during the rising phase at this flare. The ratio of flux in NUV to white light at the gradual brightening was ~ 0.49 , which may suggest that the temperature of the blackbody is low ($< 9000 \text{ K}$) or the maximum energy flux of a nonthermal electron beam is less

than $5 \times 10^{11} \text{ erg cm}^{-2} \text{ s}^{-1}$. Our simultaneous observations of NUV and white-light flare raise the issue of a simple estimation of UV flux from optical continuum data by using a blackbody model.

Key words: stars: activity — stars: flare — stars: mass-loss

1 Introduction

The Sun and cool stars suddenly release magnetic energy stored around star spots in the form of flares. A flare emits a wide range of radiation from radio waves to X-rays. Part of magnetic energy is used for plasma ejections called prominence eruptions (Sinha et al. 2019). When the velocity of them is sufficiently large, solar prominence eruptions often lead to coronal mass ejections (CMEs) (e.g., Shibata & Magara 2011). The extent to which the flare, prominence, and CME relationships that have been established for the Sun are valid for other stars is not fully understood. Therefore, observational studies of them on stars are actively being conducted.

In the last ten years, optical spectroscopic studies have shown that chromospheric lines during stellar flares sometimes show “blueshifts” or “blue asymmetries”, which indicate plasma motion toward us (Vida et al. 2016; Honda et al. 2018; Vida et al. 2019; Muheki et al. 2020a; Muheki et al. 2020b; Maehara et al. 2021; Lu et al. 2022; Namekata et al. 2022a; Inoue et al. 2023; Notsu et al. 2023; Namekata et al. 2023). These results would suggest that CMEs occur in conjunction with flares not only on the Sun but also on other stars (Leitzinger & Odert 2022; Namekata et al. 2022b). Some stellar flares and CMEs are much larger than those of the Sun (e.g., Inoue et al. 2023), and their mechanisms are not well understood. Since there are still few multiwavelength examples of stellar flares, it is imperative to accumulate simultaneous coverage of flares in X-rays, UV, and radio band together with optical detection of blueshifts of chromospheric lines.

One of the main motivations for studying stellar magnetic activity is to evaluate its impact on exoplanets (Osten & Wolk 2015; Airapetian et al. 2020). X-rays and UV radiation of stellar flares and high-energy particles produced by CMEs affect chemical compositions and escape rates of the atmosphere of exoplanets (e.g., Airapetian et al. 2016; Segura 2018; Konings et al. 2022). Mulikidjanian et al. (2003) also suggests that UV emission gives the selective advantage to the genesis of DNA and RNA of life by modeling the polymerization. Thus we need to increase our knowledge of the CME characteristics obtained by optical spectroscopy and high-energy observations (X-ray and UV).

Simultaneous observations, especially in near ultraviolet (NUV; 1600–3500 Å) and white light (6000–10000 Å), can also contribute to understanding of the flare spectral model. Though the spectral energy distribution of optical-to-NUV flares has been assumed to be a single-temperature blackbody component at $\sim 10^4 \text{ K}$ ($\simeq 0.86 \text{ eV}$) (Mochnecki & Zirin 1980; Hawley & Fisher 1992), recent NUV/white-light simultaneous observations have shown that this simple blackbody model can not adequately describe the observed spectra (Kowalski et al. 2013; Kowalski et al. 2016; Kowalski et al. 2019; Brasseur et al. 2023; Jackman et al. 2023). Furthermore, some fast (second-scale) optical photometric observations of stellar flares have been conducted (Kowalski et al. 2016; Aizawa et al. 2022; Howard & MacGregor 2022). The new 20 second cadence mode of Transiting Exoplanet Survey Satellite (TESS; Ricker et al. 2015) mission revealed substructures during the rise phase of the white-light flare in many cases (Howard & MacGregor 2022). The effect of the UV flare component on exoplanet has been discussed based on only existing optical data (Feinstein et al. 2020; Howard et al. 2020), whereas the substructure in white-light flares has yet to be investigated in detail compared with the NUV flare.

In this study, we simultaneously performed X-ray observations (0.2–12 keV), NUV observations (1600–3500 Å), optical photometric observations (6000–10000 Å) and optical spectroscopic observations (6350–6800 Å) to an active M-dwarf star EV Lac. The observation and data reduction (Section 2), analysis and results (Section 3), and discussion and conclusions (Section 4) on the details of the flare and the associated H α blueshift obtained through the simultaneous multiwavelength observations are reported in this paper.

2 Observation and Data Reduction

2.1 Target Star

EV Lac (GJ 873) is an M4.5 Ve star. Many stellar flares have been detected from EV Lac with X-ray (e.g., Favata et al. 2000) and optical (e.g., Honda et al. 2018) observations. Some studies investigated the flare frequency of EV Lac (Muheki et al. 2020b; Paudel et al. 2021; Ikuta et al. 2023). Table 1 in Paudel et al. (2021) summarizes the

Table 1. The observation log of EV Lac during our campaign (2022-10-24 to 2022-10-27)

Observation	Telescope	Obs. ID	Obs. Start time (UTC)	Exposure (ks)
X-ray	NICER (0.2–12 keV)	5100420101	2022-10-25 13:10	3.20
		5100420102	2022-10-26 12:04	5.80
		5100420103	2022-10-27 12:50	3.91
	Swift/XRT (0.2–10 keV)	00031397005	2022-10-24 12:14	1.64
		00031397006	2022-10-24 15:31	0.86
		00031397007	2022-10-25 12:07	1.65
		00031397008	2022-10-25 15:27	0.82
		00031397009	2022-10-26 12:07	0.39
		00031397010	2022-10-26 13:32	1.32
		00031397011	2022-10-26 15:10	0.82
		00031397012	2022-10-27 11:55	0.48
		00031397013	2022-10-27 13:31	1.44
		00031397014	2022-10-27 15:06	0.96
		NUV	Swift/UVOT (1600–3500 Å / UVW2)	00031397006
00031397007	2022-10-25 12:08			1.66
00031397008	2022-10-25 15:27			0.82
00031397009	2022-10-26 12:07			0.46
00031397011	2022-10-26 15:10			0.82
Optical photometry	TESS (6000–10000 Å)	—*	—*	—*
Optical spectroscopy	Nayuta/MALLS (6350–6800 Å)	—	2022-10-24 11:21	$0.3 \times 26 + 0.18 \times 81$ †
		—	2022-10-25 12:22	0.18×105 †
		—	2022-10-26 11:00	0.18×120 †
		—	2022-10-27 11:45	0.18×110 †

* TESS (Sector 57 in Cycle 5) always observed EV Lac at 20 sec cadence during our campaign.

† This means “exposure of each frame” \times “the number of frame”. Since the weather at the Nishi-Harima Astronomical Observatory was unstable on October 24, we set the exposure time to 300 seconds for each frame during cloudy conditions.

basic physical parameters of EV Lac. The distance to EV Lac is 5.05 pc (Gaia Collaboration et al. 2018), and we use this value throughout in our paper. Honda et al. (2018), Muheki et al. (2020b), and Notsu et al. (2023) discovered a $\sim 100 \text{ km s}^{-1}$ blueshift of H α line on EV Lac. Blueshifts of X-ray lines on EV Lac, which may be attributed to prominence eruptions or chromospheric evaporation, are also reported in Chen et al. (2022). Since these observations were only in one band, the total energy distribution of the flare and prominence eruption was unknown.

2.2 Multiwavelength Observations

We conducted a 4-day multiwavelength (X-ray, NUV, optical photometry, and optical spectroscopy) observation campaign of EV Lac on 2022 October 24–27. Observation times of all telescopes are summarized in Table 1.

2.2.1 NICER: X-ray

We used NASA’s Neutron Star Interior Composition Explorer (NICER; Gendreau et al. 2016) to conduct soft X-ray (0.2–12 keV) observations of EV Lac via our request to a ToO program. NICER performed monitoring on EV Lac for three days from October 25 to 27 (See Table 1). On each day, NICER made 3–5 observations, of which exposure time was ~ 1 ks each.

We retrieved observation data from HEASARC Archive. We employed the standard data analysis procedure of NICER. At first, we used `nicer12` in HEASoft ver. 6.30.1 to filter and calibrate raw data using the calibration database (CALDB) version `xti20221001`. Filtered data were barycenter corrected using `barycorr` at the target position of (RA, DEC) = (341.707214, 44.333993). Then, we extracted light curves from the filtered and barycenter-corrected event file with `xselect`. We also generated source and background spectra with `nibackgen3C50` (Remillard et al. 2022). We produced the response files, i.e., `RMF` and `ARF` files, using `nicerrmf` and `nicerarf`

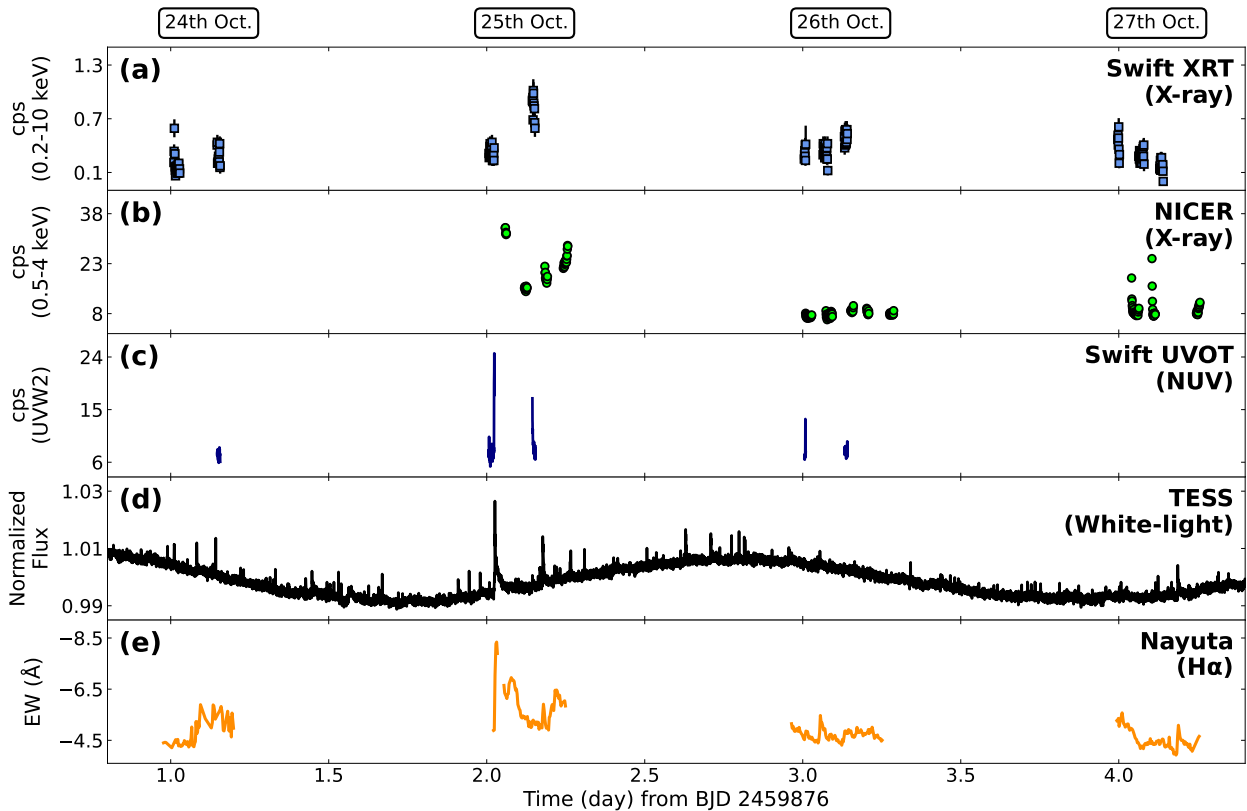


Fig. 1. Four-days light curves of EV Lac during our observation campaign on 2022 October 24–27. The time-zero of 2459876 BJD corresponds to 2022 October 23 11:53 UTC. (a) Swift XRT count rates (counts s^{-1}) in 0.2–10 keV. The time bin and error bars are 64 seconds and one standard deviation statistical error, respectively. (b) NICER count rates (counts s^{-1}) in 0.5–4 keV. The time bin and error bars are 64 seconds and one standard deviation statistical error, respectively. (c) Swift UVOT count rates (counts s^{-1}) in the UVW2 band (1600–3500 Å). The time bin is 20 seconds. (d) TESS white-light light curve shown at 6000–10000 Å. The flux is normalized by the median value. The time bin is 20 seconds. (e) Nayuta $\text{H}\alpha$ -line light curve. The equivalent width (Å) is negative values for the emission line flux in this light curve. The time bin is 180 seconds except for during the part of October 24.

commands, respectively. `XSPEC ver. 12.12.1` (Arnaud 1996) was used for our spectral analysis.

2.2.2 Swift XRT: X-ray

NASA’s Neil Gehrels Swift Observatory (Swift) also observed EV Lac in soft X-ray (0.2–10 keV) on October 24–27 via our ToO request. Swift performed 2–3 observations per day with the X-ray telescope (XRT; Burrows et al. 2005) in Photon Counting (PC) mode.

Data reduction was conducted in the same manner as that in Paudel et al. (2021) with `barycorr`, `xrtpipeline`, `xselect`. The source and background region were set to a 30-pixels (71 arcsec) radius circle and an annular extraction region with inner and outer radii of 40 (94 arcsec) and 70 (165 arcsec) pixels, respectively. Both region’s center was set to the position of the source. We used `swxpc0to12s6_20130101v014.rmf` available in the CALDB file for the response file. We produced ARF files using `xrtmkarf`. Spectral analysis was also conducted by using `XSPEC ver. 12.12.1` (Arnaud 1996).

2.2.3 Swift UVOT: NUV

Swift UVOT also observed EV Lac with UVW2 filter during almost the same time period as the XRT observation. In some observations (Obs-IDs 00031397005, 00031397010, 00031397012, 00031397013, and 00031397014), EV Lac was located outside the field of view of UVOT. UVW2 filter passes NUV light. The central wavelength and FWHM of UVW2 filter are 1928 Å and 657 Å, respectively (Poole et al. 2008).

Data reduction was conducted in the same manner as that in Paudel et al. (2021) with `coordinator`, `uvotscreen`, `barycorr`, and `uvotevtlc`. Only for the Obs-ID 00031397007, we set `uvotscreen` filtering as `evexpr=(QUALITY%256).eq.0` after confirming with the Swift helpdesk because the vast majority of events indicate `QUALITY=256`. When we created the light curve with `uvotevtlc`, time bin (`timedel`) was set to 20 seconds, the same as that of the TESS light curve.

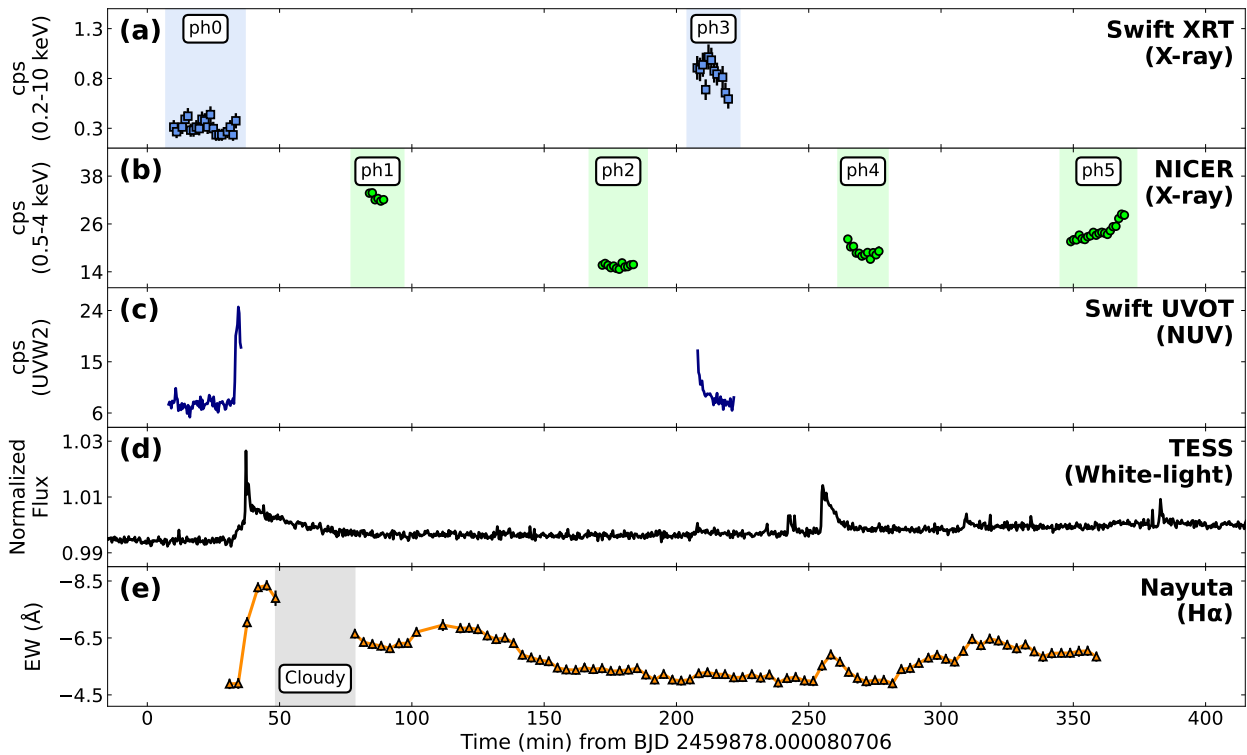


Fig. 2. Enlarged light curves of EV Lac on 2022 October 25. The time-zero of 2459878.000080706 BJD corresponds to 2022 October 25 11:52 UTC. Phase numbers in our X-ray spectral analysis are shown as “ph *” in panel (a) and (b). The gray zone in panel (e) is cloudy time.

2.2.4 TESS: Optical Photometry

TESS conducted optical photometric observations of EV Lac in Sector 57 during Cycle 5 for one month (2022 September 30–October 29) with the 20 second cadence. The band of TESS filter is 6000–10000 Å. We downloaded the observation data from the MAST data archive at the Space Telescope Science Institute (STScI). We read and analyzed the Pre-search Data Conditioning Simple Aperture Photometry (PDCSAP flux) in the data by using `python` ver. 3.9.12 and `astropy` ver. 5.0.4.

2.2.5 Nayuta: Optical Spectroscopy

We conducted optical spectroscopic observations of EV Lac with Nayuta. Nayuta is 2m telescope at the Nishi-Harima Astronomical Observatory in Japan. We used a spectrometer of Medium And Low-dispersion Long-slit Spectrograph (MALLS), whose wavelength resolution ($R = \lambda/\Delta\lambda$) is ~ 10000 at 6500 Å. MALLS covers 6350–6800 Å including the H α line. During most of the time, the exposure time of each frame was set to 180 seconds, but on the first day (October 24), it was occasionally increased to 300 s due to unstable weather conditions.

Data processing was conducted in the same manner as that in Honda et al. (2018) using `IRAF`¹ package (Today

1986). We made a minor adjustment to the wavelength calibration by using photospheric line profiles after the `IRAF` processing.

3 Analysis and Results

3.1 Light Curves

Multiwavelength light curves of EV Lac obtained by our campaign are shown in Figure 1. A large flare, which is the focus of this paper, occurred on October 25. The white-light light curve shows that many small flares occur everyday on EV Lac.

Figure 2 shows enlarged light curves on October 25. We numbered each observation of Swift/XRT and NICER as “Phase (ph) *”. As shown in Figure 2, the largest flare, which is the focus of this paper, started at 12:28 UTC on 2022 October 25, corresponding to ~ 40 min from the time origin of Figure 2. We have succeeded in observing the rising phase of the flare in NUV, white light, and H α . At the end of Phase 0, UV and white light were already increasing, but X-ray rising was not observed. Other small flares also occurred, e.g., the X-ray and UV flare at ~ 210 min (Phase 3), and the white-light and H α recorded flare at

are operated by the Association of Universities for Research in Astronomy, Inc., under cooperate agreement with the National Science Foundation.

¹ IRAF is distributed by the National Optical Astronomy Observatories, which

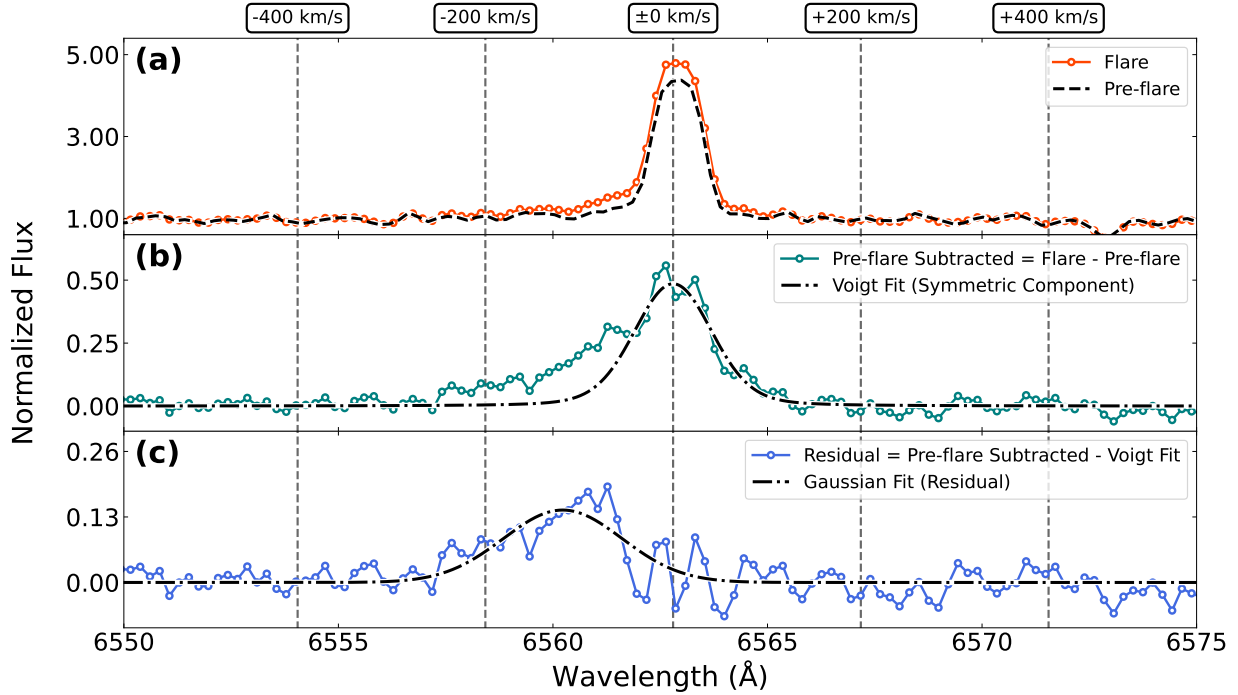


Fig. 3. An example of normalized $H\alpha$ spectra extracted from the time period of 127–129 min in the light curve of Figure 2. Gray vertical dashed lines show Doppler velocity from the line center at 6562.8 Å. (a) Comparison of the continuum at the 127–129 min range (orange solid line) with that in the pre-flare data at the 30–35 min (black dashed line). (b) Pre-flare subtracted spectrum of panel (a). The black dashdot line represents the Voigt function fitting only used for the red side of the line center (6562.8–6600 Å). (c) Residual between the pre-flare subtracted spectrum (panel b) and the best-fit Voigt function result in panel (b). The black dashdot line represents the Gaussian fitting.

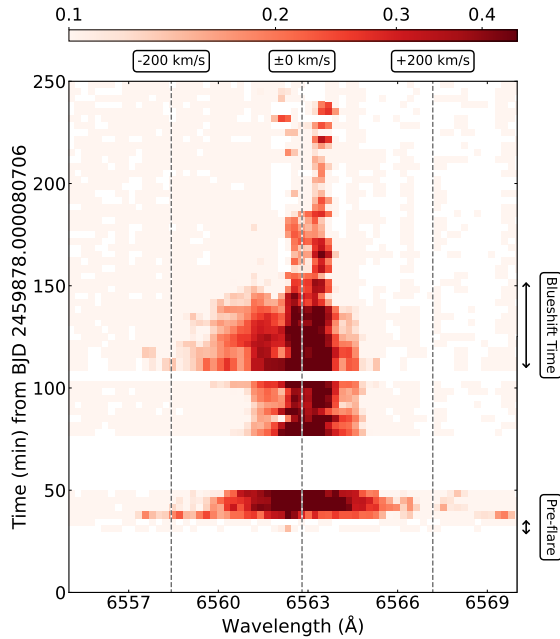


Fig. 4. Time variation of pre-flare subtracted spectrum. The horizontal and vertical axes represent the wavelength and time, respectively. The time origin is the same as Figure 2. The red color scale indicates flux normalized by the continuum. Gray dashed lines show Doppler velocity from the line center (6562.8 Å).

~250 min slightly before Phase 4. Though there is no large flare in the white-light light curve before and after Phase 5, emission of X-ray and $H\alpha$ is gradually increasing after ~300 min. Compared to white light, other wavelength emission has greater flare contrast. In addition, there are flares where emission is observed only in X-ray and UV (e.g., the X-ray and UV flare at ~210 min). Hereafter, we focus on the largest flare during our observation campaign.

3.2 Spectral Analysis

3.2.1 $H\alpha$

We searched the largest flare for an asymmetric component of $H\alpha$ in the same manner as Inoue et al. (2023). Figure 3 shows the $H\alpha$ spectrum extracted from a frame at 127–129 min (Figure 2). At first, we created the “pre-flare” spectrum shown as black dashed line in Figure 3a by combining two frames just before the flare start. Then, subtracting the pre-flare spectrum from the flare spectrum (127–129 min), we made pre-flare-subtracted spectrum (Figure 3b). Since a blue-shifted excess component was confirmed (Figure 3b) at ~6560 Å (-100 km s^{-1}), we separated it from a symmetric component by fitting only the red side of $H\alpha$ with the Voigt function. The line center of the Voigt function was fixed to the $H\alpha$ line cen-

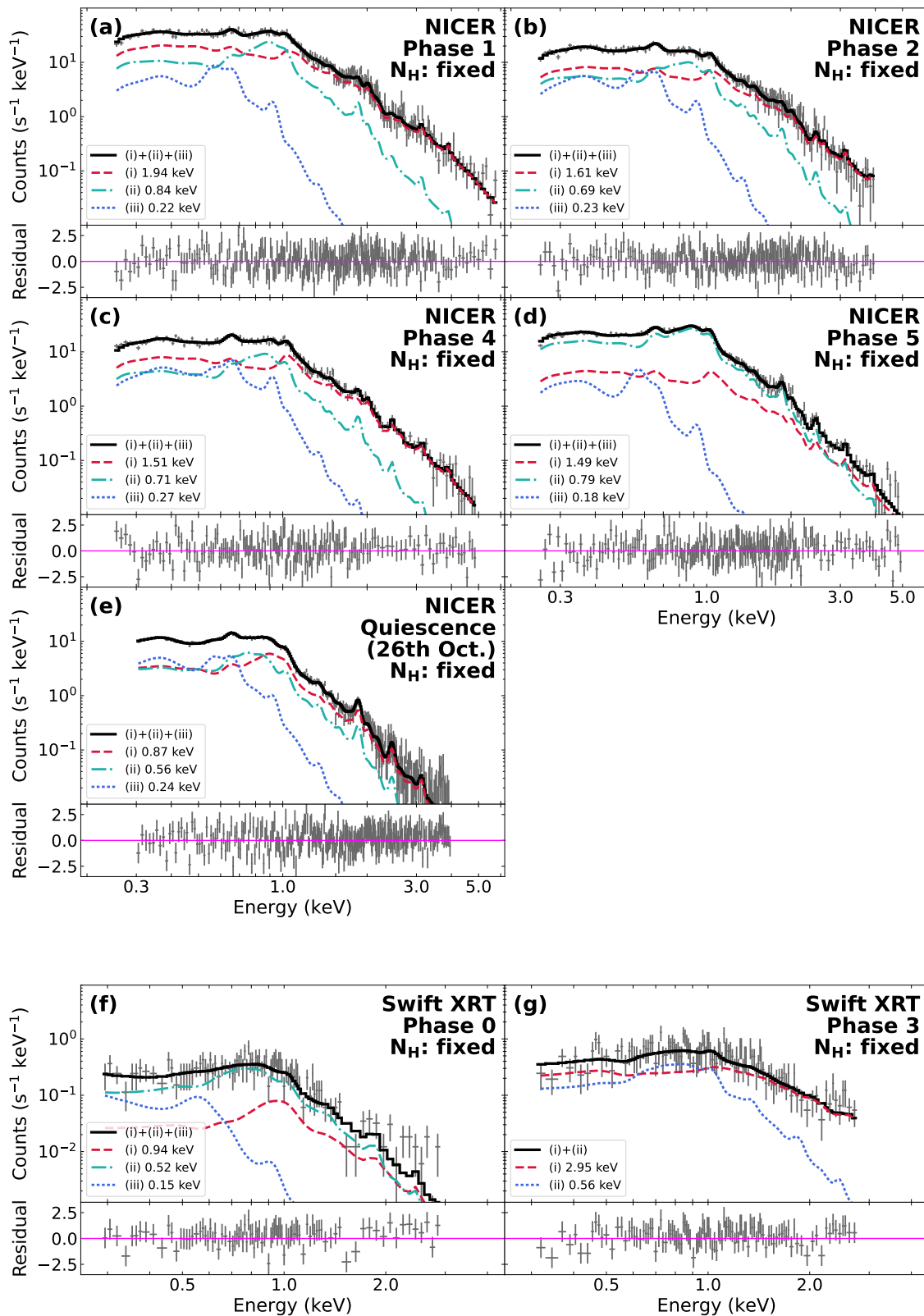


Fig. 5. Background-subtracted and response-uncorrected X-ray spectra at each phase shown in Figure 2. The best-fit curves for three-temperature vavpec models are shown by solid black lines. Red dashed, green dashdot, and blue dotted lines represent the high, medium, and low temperature component, respectively. Panels (a-d) and (g) are spectra during the flare, whereas panels (e) and (f) are spectra during the quiescence.

Table 2. Best-fit parameters of all spectra with three temperature collisionally-ionized models*

	NICER					Swift XRT		
	Phase 1	Phase 2	Phase 4	Phase 5	Oct 26	Phase 0	Phase 3	
Exposure (ks)	0.42	0.71	0.71	1.19	5.80	1.65	0.82	
tbabs								
N_{H} (10^{18} cm $^{-2}$)	4.0	4.0	4.0	4.0	4.0	4.0	4.0	
vapec (High Temp.)								
Temperature	kT (keV)	$1.94_{\pm 0.08}$	$1.61_{\pm 0.06}$	$1.51_{\pm 0.06}$	$1.49_{\pm 0.09}$	$0.87_{\pm 0.04}$	$0.94_{\pm 0.35}$	$2.95_{\pm 1.42}$
	T (MK)	$22.5_{\pm 0.9}$	$18.8_{\pm 0.7}$	$17.6_{\pm 0.7}$	$17.3_{\pm 1.0}$	$10.1_{\pm 0.5}$	$10.9_{\pm 4.1}$	$34.2_{\pm 16.5}$
norm (10^{-2})	$2.60_{\pm 0.11}$	$0.94_{\pm 0.05}$	$0.88_{\pm 0.04}$	$0.50_{\pm 0.07}$	$0.49_{\pm 0.10}$	$0.11_{\pm 0.15}$	$1.20_{\pm 0.16}$	
vapec (Medium Temp.)								
Temperature	kT (keV)	$0.84_{\pm 0.02}$	$0.69_{\pm 0.03}$	$0.71_{\pm 0.04}$	$0.79_{\pm 0.01}$	$0.56_{\pm 0.05}$	$0.52_{\pm 0.14}$	—
	T (MK)	$9.74_{\pm 0.23}$	$8.00_{\pm 0.35}$	$8.24_{\pm 0.46}$	$9.16_{\pm 0.12}$	$6.50_{\pm 0.58}$	$6.03_{\pm 1.62}$	—
norm (10^{-2})	$1.15_{\pm 0.16}$	$0.55_{\pm 0.09}$	$0.42_{\pm 0.08}$	$1.58_{\pm 0.10}$	$0.43_{\pm 0.07}$	$0.43_{\pm 0.16}$	—	
vapec (Low Temp.)								
Temperature	kT (keV)	$0.22_{\pm 0.03}$	$0.23_{\pm 0.01}$	$0.27_{\pm 0.02}$	$0.18_{\pm 0.03}$	$0.24_{\pm 0.01}$	$0.15_{\pm 0.10}$	$0.56_{\pm 0.13}$
	T (MK)	$2.55_{\pm 0.35}$	$2.67_{\pm 0.12}$	$3.13_{\pm 0.23}$	$2.09_{\pm 0.35}$	$2.78_{\pm 0.12}$	$1.74_{\pm 1.16}$	$6.20_{\pm 1.44}$
norm (10^{-2})	$0.24_{\pm 0.09}$	$0.21_{\pm 0.04}$	$0.21_{\pm 0.04}$	$0.10_{\pm 0.02}$	$0.26_{\pm 0.03}$	$0.15_{\pm 0.10}$	$0.52_{\pm 0.12}$	
Z (Z_{\odot})	He	1.00	1.00	1.00	1.00	1.00	1.00	1.00
	C	$0.59_{\pm 0.09}$	$0.52_{\pm 0.06}$	$0.53_{\pm 0.05}$	$0.63_{\pm 0.08}$	$0.44_{\pm 0.02}$	0.44	0.52
	N	$0.59_{\pm 0.09}$	$0.52_{\pm 0.06}$	$0.53_{\pm 0.05}$	$0.63_{\pm 0.08}$	$0.44_{\pm 0.02}$	0.44	0.52
	O	$0.59_{\pm 0.09}$	$0.52_{\pm 0.06}$	$0.53_{\pm 0.05}$	$0.63_{\pm 0.08}$	$0.44_{\pm 0.02}$	0.44	0.52
	Ne	1.00	1.00	$1.28_{\pm 0.27}$	1.00	$0.45_{\pm 0.07}$	0.45	1.00
	Mg	$0.23_{\pm 0.13}$	$0.41_{\pm 0.12}$	$0.34_{\pm 0.12}$	$0.29_{\pm 0.05}$	$0.24_{\pm 0.04}$	0.24	0.41
	Al	1.00	1.00	1.00	1.00	1.00	1.00	1.00
	Si	$0.48_{\pm 0.10}$	$0.30_{\pm 0.09}$	$0.50_{\pm 0.10}$	$0.34_{\pm 0.04}$	$0.40_{\pm 0.04}$	0.40	0.30
	S	$0.15_{\pm 0.14}$	$0.41_{\pm 0.16}$	$0.59_{\pm 0.16}$	$0.42_{\pm 0.10}$	$0.46_{\pm 0.09}$	0.46	0.41
	Ar	1.00	1.00	1.00	1.00	1.00	1.00	1.00
	Ca	1.00	1.00	1.00	1.00	1.00	1.00	1.00
	Fe	$0.21_{\pm 0.04}$	$0.13_{\pm 0.03}$	$0.18_{\pm 0.03}$	$0.13_{\pm 0.01}$	$0.14_{\pm 0.01}$	0.14	0.13
Ni	1.00	1.00	1.00	1.00	1.00	1.00	1.00	
χ^2 (<i>d.o.f</i>)	252 (247)	192 (216)	194 (156)	232 (200)	290 (259)	71 (87)	87 (107)	

* The error ranges correspond to 90% confidence level. Values without errors mean that they are fixed.

ter (6562.8 Å). Figure 3c shows the residual between the pre-flare subtracted spectrum and the Voigt function fitted only on the red side. Finally, we fit the residual with Gaussian. We conducted this Voigt fitting of the symmetric components for all frames on October 25. We also performed the Gaussian fitting of the blue-shifted excess components for 10 frames at 112–145 min, when they are clearly present. The line center and standard deviation (σ) of the Gaussian fitted on the blue-shifted excess components were 6558–6560 Å ($-200 \sim -100$ km s $^{-1}$) and ~ 1 Å (~ 45 km s $^{-1}$), respectively.

Figure 4 shows the time variation of the pre-flare subtracted spectrum. As shown in 110–150 min in Figure 4, there was a continuous blueshifted excess component in

the H α emission line. The blue-shifted excess component appeared one hour after the flare peak. It coincides with the secondary peak at 112 min of the H α light curve (see Figure 2e).

3.2.2 X-ray

We show in Figure 5 the NICER and Swift X-ray spectra of each phase on October 25. We also extracted the NICER spectrum on October 26 as a quiescent data (Figure 5e), since there is no X-ray flare observed during this period. The Phase 0 spectrum obtained by Swift XRT is also a quiescent spectrum because the X-ray flare started after the end of Phase 0.

In order to investigate the time variation of temperature, abundance, and emission measure during the flare,

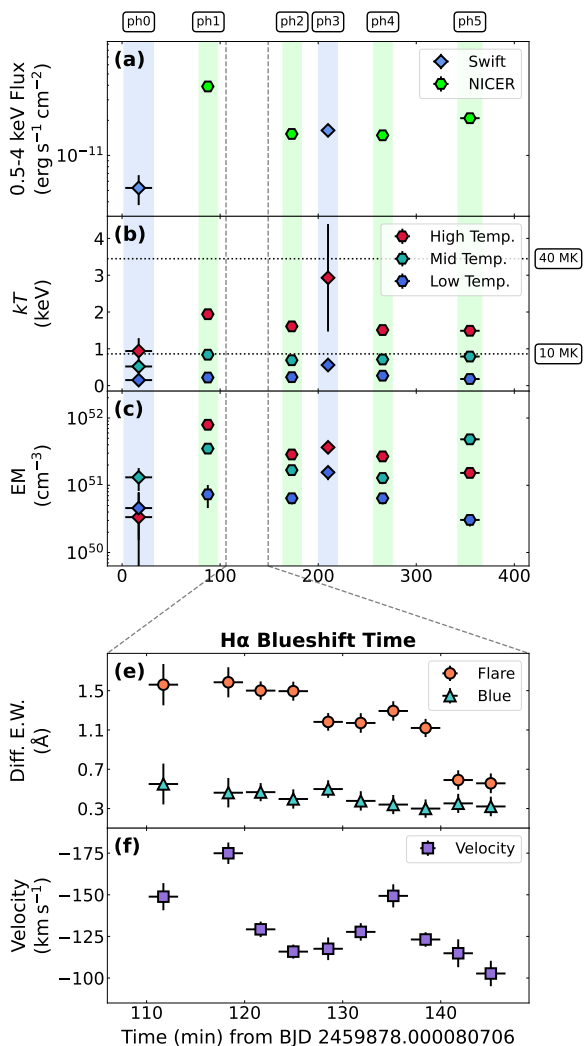


Fig. 6. Time evolution of physical parameters obtained by the X-ray and H α spectral analysis. (a) Time variation of 0.5–4 keV X-ray flux. Blue diamonds and lime hexagons indicate the 0.5–4 keV flux calculated from Swift and NICER X-ray spectra, respectively. Phase numbers are also shown in the same manner as in Figure 2. The area sandwiched between gray horizontal lines corresponds to the time period when H α line was blue-shifted. (b) Temperatures of plasma. Red, green, and blue markers indicate high, medium, and low temperature components, respectively. Diamonds and hexagons corresponds Swift and NICER data, respectively. (c) Emission measure with colors and markers the same as in panel (b). (d) Light curves of the equivalent width of H α during it was blueshifted. The orange circles and turquoise triangles indicate the equivalent widths of the flare symmetric and blueshifted excess components, respectively. (e) Corresponding velocity of the blueshifted excess components of H α .

we performed X-ray spectral fitting for all the spectra utilizing with three temperature collisionally-ionized equilibrium components (*vaptec*) with interstellar absorption (*tbabs*). Note that although we also tried a single- or two-temperature *vaptec* model, they give a statistically unacceptable fit. Only for the Phase 3 spectrum, we used two-temperature *vaptec* model because the best-fit parameter

of temperature with three-temperature *vaptec* model was physically unacceptable. We linked abundance among the three components and further tied the abundance of C, N and O, which have the similar first ionization potential. We fixed the hydrogen column density at $N_{\text{H}} = 4.0 \times 10^{18} \text{ cm}^{-2}$ (Paudel et al. 2021), since the small distance, 5.05 pc (Gaia Collaboration et al. 2018), to the source prevents us from determining the small interstellar absorption from the observed data. Due to a lack of statistics, it was difficult to determine abundance of Phase 0 and 3 spectra obtained by Swift XRT. Therefore, abundances of Phase 0 and 3 were fixed to the best-fit value of October 26 NICER spectrum and Phase 2, respectively. Figure 5 and Table 2 summarizes the spectral fitting and its best-fit parameters, respectively.

As an alternative spectral modeling, we also conducted fitting with the fixed quiescent component and two temperature collisionally-ionized models (*vaptec*) with interstellar absorption (*tbabs*) for flare spectra (Phase 1-5). In the fitting, we could not fit Phase 2-4 spectra with fixed N_{H} . Since the best-fit parameters of temperature were physically unacceptable in this modeling, we did not adopt this modeling. See the Appendix. for more information about the fitting with the fixed quiescent component.

3.2.3 Time evolution of fitting parameters

Figure 6 shows the time evolution of physical parameters obtained by our X-ray and H α spectral analysis. From Phase 1 to Phase 2, the plasma temperature and emission measure of the large flare is cooling and decreasing as indicated in Figure 6a–c. As the light curve in Figure 2 also showed, flux, temperature, and emission measure remained higher than those in pre-flare (Phase 0) even after Phase 2 because some other small flares occurred. This suggests that these small flares injected energy into the plasma.

As shown in Figure 6e, we investigated time variation of the equivalent widths of H α line, and decomposed them into the flare symmetric component and the blueshifted excess component. We also calculated the Doppler velocity of the blueshifted excess component (Figure 6f). The equivalent widths of the flare and blueshifted excess components were calculated by integrating Voigt function (cf. Figure 3b) and Gaussian (cf. Figure 3c), respectively. The Doppler velocity of the blueshifted excess component corresponds to the wavelength of the center of Gaussian (cf. Figure 3c). The equivalent width of the blueshifted excess component was $\sim 1/3$ of the flare symmetric component at ~ 110 min. Then, both components were decaying and the difference became progressively smaller. Time variation of the Doppler velocity of the blueshifted excess component appears to have two peaks at ~ 120 and ~ 135 min.

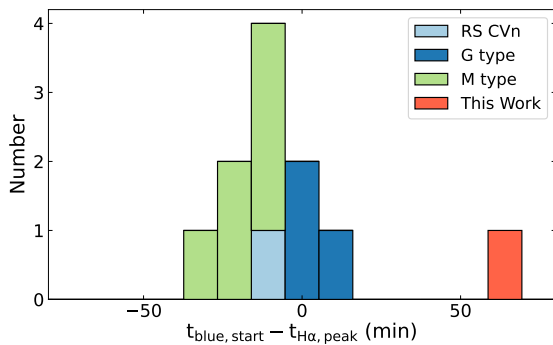


Fig. 7. Distribution of the difference between the appearance time of H α blue-shifted components ($t_{\text{blue,start}}$) and flare peak ($t_{\text{H}\alpha,\text{peak}}$). Light blue, blue and green correspond to H α blue-shift events on RS CVn (Inoue et al. 2023), G (Namekata et al. 2022a; Namekata et al. 2023), and M (Vida et al. 2016; Honda et al. 2018; Maehara et al. 2021; Notsu et al. 2023) type stars, respectively. Orange corresponds to this work.

These velocities of $100 - 200 \text{ km s}^{-1}$ are comparable to the blueshift on mid M dwarf stars (Honda et al. 2018; Vida et al. 2019; Notsu et al. 2023).

4 Discussion

4.1 Blue-shifts and prominence eruptions

The H α blue shifted excess components were identified during the flare (Section 3.2.1, Figure 3 & 4). The stellar rotational velocity ($v \sin i \sim 3.5 \text{ km s}^{-1}$; Reiners et al. 2018) can not explain the observed blueshifts ($\sim 100 \text{ km s}^{-1}$).

There are two candidates for such moving plasma. The one is a chromospheric temperature (cool) upflow associated with chromospheric evaporation (Tei et al. 2018) and the other is a prominence eruption (Otsu et al. 2022). Since we could not observe signs of the mass ejection in X-ray and UV, such as the coronal dimming (Veronig et al. 2021; Loyd et al. 2022) and the increase of the hydrogen density (Moschou et al. 2017; Moschou et al. 2019), we can not assure that the observed blue-shifts are attributed to the prominence eruption. However, the velocity of cool upflow ($\sim 10 \text{ km s}^{-1}$; Tei et al. 2018) is typically smaller than the observed velocity ($\sim 100 \text{ km s}^{-1}$) in the case of solar flares. Furthermore, there was no significant increase in white light when the blue-shifts appeared. According to numerical simulations, the injection of non-thermal electrons into deep chromosphere can produce unheated cool upward flows above the chromospheric evaporation. Such non-thermal electrons are also expected to produce chromospheric condensation, producing significant white-light emissions (e.g., Li et al. 2023). The lack of white-light emission therefore may indicate that the above process is not working.

Honda et al. (2018) also discussed the possibility of the

absorption by post-flare loops making the blue asymmetry during the decay phase. However, the H α spectra in this study did not show a sharp red-shifted absorption as observed by Honda et al. (2018).

For these reasons, it is highly probable that the prominence eruption occurred and made the observed blue-shifted excess components.

4.1.1 Timing of the prominence eruption

One interesting point in the present event is the timing of H α blue-shift. In many cases, blue-shifted excess components of H α are pronounced at the flare peak (Figure 7)². In other words, most prominence eruptions are initiated at the flare peak. However, the prominence discovered in this study appeared ~ 1 hour after the peak of the flare. There are three possible cases for interpreting the delay of the H α blue-shift.

First, another flare occurred ~ 1 hour after the peak of the first flare. There is no obvious signs of another flare in the white-light (Figure 2d), while there are tiny enhancements in H α line center emission (Figure 4). It is possible that a non-white light flare accompanied by a mass ejection occurred. It is also possible that the prominence erupted with no flare connections. Some studies have reported the prominence eruption without obvious flare connections on the Sun (Zirin 1969; Mason et al. 2021).

Second, the prominence erupted during the decay phase of the flare. Kurokawa et al. (1987) reported an X13 class solar flare in which a filament erupted about 40 minutes later than the major flare peak. The change of magnetic field configuration due to the flare reconnection should make a twisted filament start to be ejected and accelerated by magnetic force in a twisted tube (Shibata & Uchida 1986). Though such delayed prominence eruptions have not been observed on stars (Figure 7), this interpretation is consistent with our observations.

Third, the prominence erupted on the disk at the flare peak and outside the limb ~ 1 hour after the flare peak. Generally, prominence eruptions on disk and outside a limb are observed as H α absorption and emission, respectively in the case of the Sun and solar-type stars (Parenti 2014; Otsu et al. 2022; Namekata et al. 2022a; Namekata et al. 2023). It is possible that the prominence initially erupted on disk and erupted outside a limb in the course of the one-hour trip. If we assume the prominence visibility on

² For the flare described in Vida et al. (2016), we took the difference between t_1 and the flare peak (cf. Figure 14 in Vida et al. 2016) because blue-shifts at t_2 and t_3 may be blue-shifts without flares (Muheki et al. 2020b). For the flare Y6 in Notsu et al. (2023), we considered time [1] in Figure 14 in Notsu et al. (2023) to be the flare peak because there were multiple peaks during the flare, which suggests that some flares occurred simultaneously.

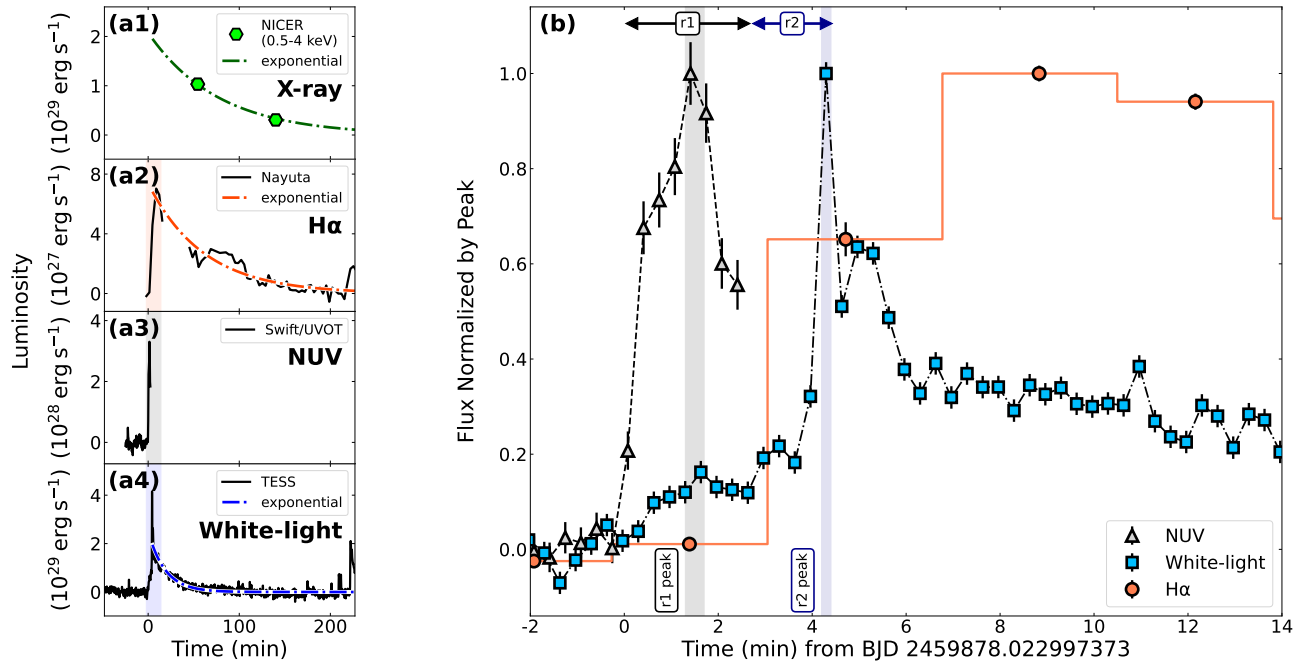


Fig. 8. (a1-a4) Quiescent-subtracted light curves. The time zero point is set to the beginning of the flare. The dashdot lines show the exponential function fitted for the decay phase of the light curve. (a1) Flare luminosity of 0.5–4 keV X-ray. (a2) Flare luminosity of H α . Note that the luminosity of the blue-shifted excess component is removed in this curve. (a3) Flare luminosity of UVW2 band (1600–3500 Å). (a4) Flare luminosity of white light (6000–10000 Å). (b) Enlarged light curves around the rising phase of the flare, which corresponds to the shaded time intervals in panel (a2–a4). All curves are normalized by their peak values. Aqua triangle, blue square, and orange circle represent NUV, white-light, and H α , respectively. Blue and green shaded regions indicate gradual and rapid phase of white-light, respectively.

M-dwarf is the same as those on the Sun and solar-type stars, this possibility is unlikely because H α spectra between the flare peak and the start of blue-shifted emission components show no signs of blue-shifted absorption components. However, Leitzinger et al. (2022) estimated that prominence on disk can be H α emission for dM stars using 1D NLTE modeling and cloud model formulation, so the source function of H α line of M-dwarf prominences could be relatively comparable to or higher than background continuum radiation. Therefore, in some specific prominence parameters, there could be a possibility that the erupted prominence is initially invisible inside the disk and appeared as an emission after going outside the stellar limb. Since we do not know the source function of M-dwarf prominence, we need to perform simultaneous observations of some Balmer lines (c.f. Vida et al. 2016; Notsu et al. 2023) in the future to verify this interpretation. Furthermore, given that the prominence moved $\sim 3.6 \times 10^5$ km ($\sim 1.5R_{\text{star}}$) and continued to expanding over \sim one hour, it is unclear whether it retains enough emission measure to be observed as H α emission at the time. Theoretical simulations are needed to investigate the time variation of emission measure of the prominence.

4.2 Physical parameters

From the results of spectral analysis in Section 3.2, we calculated basic physical parameters of the flare and prominence.

4.2.1 Prominence Mass

We estimated the mass of the prominence using a method used by Maehara et al. (2021), Inoue et al. (2023), and Notsu et al. (2023). As shown in Figure 6e, the maximum equivalent width of the blueshifted excess component is ~ 0.5 Å. The equation (5) in Notsu et al. (2023) presented the formula to convert the equivalent width ($EW_{\text{H}\alpha}$) of H α to its luminosity,

$$L_{\text{H}\alpha}(t) = 4\pi d^2 \times F_{\text{H}\alpha}^{\text{cont}} \times EW_{\text{H}\alpha}(t), \quad (1)$$

where $F_{\text{H}\alpha}^{\text{cont}}$ ($5.7 \times 10^{-13} \text{ erg cm}^{-2} \text{ s}^{-1} \text{ \AA}^{-1}$; Notsu et al. 2023) is the quiescent flux density at the continuum level around H α of EV Lac, and d (5.05 pc; Gaia Collaboration et al. 2018) is the distance between the Earth and the target star. Using Equation (1), we calculated the luminosity of the blueshifted excess component L_{blue} :

$$L_{\text{blue}} \sim 8 \times 10^{26} \text{ erg s}^{-1}. \quad (2)$$

We adopted the non-local thermodynamic equilibrium (NLTE) model of the solar prominence (Heinzel et al. 1994)

and the range of the optical thickness τ_p of H α line center is assumed to be $0.1 < \tau_p < 100$ as done in Inoue et al. (2023).

1. $\tau_p \sim 0.1$: NLTE model (Heinzl et al. 1994) indicates that the H α flux of the prominence per unit time, unit area, and unit solid angle $F_{\text{H}\alpha}$ is

$$F_{\text{H}\alpha} \sim 10^4 \text{ erg s}^{-1} \text{ cm}^{-2} \text{ sr}^{-1}. \quad (3)$$

As shown in Equation (8) in Inoue et al. (2023), L_{blue} is expressed as

$$L_{\text{blue}} = \int \int F_{\text{H}\alpha} dA d\Omega = 2\pi A_p F_{\text{H}\alpha}, \quad (4)$$

where A_p is the area of the region emitting H α . Using Equations (2)–(4), we obtained

$$A_p \sim 1 \times 10^{22} \text{ cm}^2 \sim 6 \times A_{\text{star}}, \quad (5)$$

where $A_{\text{star}} = \pi R_{\text{star}}^2$ ($\sim 2 \times 10^{21} \text{ cm}^2$) is the area of the hemisphere of the star and R_{star} ($\sim 3 \times 10^{10} \text{ cm}$; Paudel et al. 2021) is the radius of the star. Heinzl et al. (1994) also indicates that in the case of Equation (3), the emission measure $n_e^2 D$ of the prominence is

$$n_e^2 D \sim 10^{28} \text{ cm}^{-5}, \quad (6)$$

where D and n_e are the geometrical thickness and the electron density of the prominence, respectively. Hirayama (1986) shows the typical electron density of a solar prominence is

$$10^{10} \text{ cm}^{-3} < n_e < 10^{11.5} \text{ cm}^{-3}. \quad (7)$$

Notsu et al. (2023) calculated the ratio between the hydrogen density n_{H} and the electron density n_e of a prominence,

$$n_e/n_{\text{H}} = 0.17 - 0.47 \quad (8)$$

from Table 1 of Labrosse et al. (2010). The mass of the prominence is expressed as

$$M \sim m_{\text{H}} n_{\text{H}} A_p D, \quad (9)$$

where m_{H} is the mass of hydrogen atom. From Equations (5)–(9),

$$1 \times 10^{15} \text{ g} < M < 1 \times 10^{17} \text{ g} \quad (10)$$

is obtained.

2. $\tau_p \sim 100$: Calculated as in case $\tau_p \sim 0.1$,

$$F_{\text{H}\alpha} \sim 10^6 \text{ erg s}^{-1} \text{ cm}^{-2} \text{ sr}^{-1}, \quad (11)$$

$$A_p \sim 1 \times 10^{20} \text{ cm}^2 \sim 6 \times 10^{-2} \times A_{\text{star}}, \quad (12)$$

$$n_e^2 D \sim 10^{31} \text{ cm}^{-5}, \quad (13)$$

$$1 \times 10^{16} \text{ g} < M < 1 \times 10^{18} \text{ g}. \quad (14)$$

We obtained the range of M from Equations (10) and (14),

$$1 \times 10^{15} \text{ g} < M < 1 \times 10^{18} \text{ g}. \quad (15)$$

This mass and the white-light bolometric flare energy $E_{\text{WLF,bol}}$ of $3.4 \times 10^{32} \text{ erg}$ (see Section 4.4) are comparable to previous blueshifts on M-dwarf stars (Moschou et

al. 2019; Maehara et al. 2021; Notsu et al. 2023) and correspond to the value expected from the flare energy-mass scaling law $M \propto E_{\text{WLF,bol}}^{2/3}$ (Takahashi et al. 2016; Namekata et al. 2022a Inoue et al. 2023; Namekata et al. 2023).

4.2.2 Flare Loop Size

Shibata & Yokoyama (2002) showed magnetic reconnection model equations for calculating the length of a flare loop L_{SY} and the flare magnetic field strength B_{SY} ,

$$L_{\text{SY}} = 10^9 \left(\frac{EM_{\text{peak}}}{10^{48} \text{ cm}^{-3}} \right)^{3/5} \times \left(\frac{n_0}{10^9 \text{ cm}^{-3}} \right)^{-2/5} \left(\frac{T_{\text{peak}}}{10^7 \text{ K}} \right)^{-8/5} \text{ cm}, \quad (16)$$

$$B_{\text{SY}} = 50 \left(\frac{EM_{\text{peak}}}{10^{48} \text{ cm}^{-3}} \right)^{-1/5} \times \left(\frac{n_0}{10^9 \text{ cm}^{-3}} \right)^{3/10} \left(\frac{T_{\text{peak}}}{10^7 \text{ K}} \right)^{17/10} \text{ G}, \quad (17)$$

where EM_{peak} is the peak volume emission measure, T_{peak} is the peak temperature, and n_0 is the preflare coronal density. Osten et al. (2006) placed a constraint on the coronal electron density of EV Lac between 10^{10} cm^{-3} and 10^{14} cm^{-3} using X-ray and UV density-sensitive line ratios. For coronal temperature during our quiescent phase (Table 2), coronal density is assumed to be $10^{11} - 10^{13} \text{ cm}^{-3}$ (see Figure 9 in Osten et al. 2006). We substituted temperature and emission measure obtained from the X-ray spectrum of Phase 1, which is closest to the flare peak, for Equations (16) and (17). As a result, the flare magnetic field strength and loop size are $80 \text{ G} < B_{\text{SY}} < 300 \text{ G}$ and $0.1 R_{\text{star}} < L_{\text{SY}} < 0.7 R_{\text{star}}$, respectively.

We also calculated the flare loop size L_{N} by using the equation derived by Namekata et al. (2017b) and Namekata et al. (2023):

$$L_{\text{N}} = 1.64 \times 10^9 \left(\frac{\tau_{\text{decay}}^{\text{WLF}}}{100 \text{ s}} \right)^{2/5} \times \left(\frac{E_{\text{WLF,bol}}}{10^{30} \text{ erg}} \right)^{1/5} \left(\frac{n_0}{n_{\odot}} \right)^{-1/5} \text{ cm}, \quad (18)$$

where $\tau_{\text{decay}}^{\text{WLF}}$ is the e -folding time of the white-light flare. The calculated value is $0.09 R_{\text{star}} < L_{\text{N}} < 0.2 R_{\text{star}}$ Table 3 compiles the results of our calculation. L_{SY} and L_{N} are

Table 3. Flare loop size and magnetic field strength estimated from X-ray spectrum of phase 1

n_0	B_{SY}	L_{SY}	L_{N}
10^{11} cm^{-3}	$\sim 80 \text{ G}$	$\sim 0.7 R_{\text{star}}$	$\sim 0.2 R_{\text{star}}$
10^{12} cm^{-3}	$\sim 160 \text{ G}$	$\sim 0.3 R_{\text{star}}$	$\sim 0.1 R_{\text{star}}$
10^{13} cm^{-3}	$\sim 300 \text{ G}$	$\sim 0.1 R_{\text{star}}$	$\sim 0.09 R_{\text{star}}$

the almost same order for each coronal density.

4.3 Multiwavelength Rising Phase Data

Figure 8b shows the enlarged light curve of the rising phase of the flare. Similar to solar flares, white light and NUV due to non-thermal emission increases faster than $H\alpha$, which is called Neupert effect (e.g., Neupert 1968; Namekata et al. 2020; Tristan et al. 2023).

The rising phase of the white-light flare consists of two phases (Figure 8b): a gradual rise (r1) and a rapid rise (r2). Howard & MacGregor (2022) showed many samples of flares which exhibit a similar substructure using 20 second cadence mode data of TESS. Our new finding in this study is that there is already a sharp increase in NUV during the white-light gradual phase (r1). The last three bins of the NUV light curve appear to have already begun to decay. Since the NUV observations stopped ~ 35 min in Figure 8, it is not clear whether the NUV flux rose sharply again or continued to decay during r2.

The ratio of NUV flux to white-light flux is crucial to the model of the broadband spectrum of stellar flares (e.g., Jackman et al. 2023; Brasseur et al. 2023). However, there are few simultaneous observations of stellar flares in NUV and white-light band. While we missed NUV flux during r2, we calculated the ratio of NUV flux to white-light one at the r1 peak.

We evaluated the luminosity at the r1 peak in the TESS band ($L_{\text{peak}}^{\text{TESS}}$) in the same manner as Notsu et al. (2023):

$$L_{\text{peak}}^{\text{TESS}} = L_{\text{quiescence}}^{\text{TESS}} \times \Delta f_{\text{peak}}^{\text{TESS}} = 6.7 \times 10^{28} \text{ erg s}^{-1}, \quad (19)$$

where $L_{\text{quiescence}}^{\text{TESS}}$ ($1.3 \times 10^{31} \text{ erg s}^{-1}$; Notsu et al. 2023) is the quiescent luminosity of EV Lac in TESS band and $\Delta f_{\text{peak}}^{\text{TESS}} = (f_{\text{TESS,p}} - f_{\text{TESS,q}})/f_{\text{TESS,q}}$ is the relative flux at the flare peak (cf. Figure 9b). $f_{\text{TESS,p}}$ and $f_{\text{TESS,q}}$ are TESS flux at the r1 peak and of quiescence, respectively. See Section 4.4 and Figure 9 for more information about the TESS flux. We also calculated the luminosity at the flare peak in UVW2 band ($L_{\text{peak}}^{\text{UVW2}}$) from the value of FLUX_AA in the light curve file created by `uvotevt1c`:

$$\begin{aligned} L_{\text{peak}}^{\text{UVW2}} &= (F_{\text{peak}}^{\text{UVW2}} - F_{\text{quiescence}}^{\text{UVW2}}) \times W_{\text{eff}}^{\text{UVW2}} \times 4\pi d^2 \\ &= 3.3 \times 10^{28} \text{ erg s}^{-1}, \end{aligned} \quad (20)$$

where $F_{\text{peak}}^{\text{UVW2}}$ and $F_{\text{quiescence}}^{\text{UVW2}}$ are flux density (FLUX_AA) at the flare peak and pre-flare, respectively. $W_{\text{eff}}^{\text{UVW2}}$ (667.73 \AA ; SVO Filter Profile Service³) is the equivalent width of the effective area of UVW2 filter, and d (5.05 pc ; Gaia Collaboration et al. 2018) is the distance between the Earth and EV Lac. From Equations (19) and (20),

³<http://svo2.cab.inta-csic.es/theory/fps/index.php?id=Swift/UVOT.UVW2&mode=browse&gname=Swift&gname2=UVOT#filter>

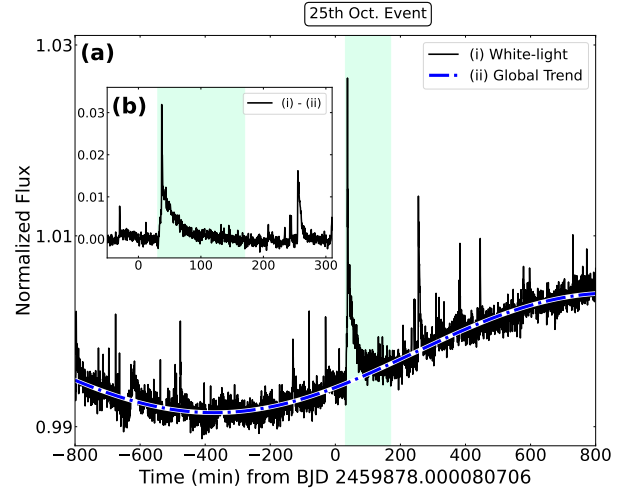


Fig. 9. White-light light curves of EV Lac observed with TESS. Time setting is the same as in Figure 2. (a) Long-term curve of EV Lac. The flux is normalized by the median value. The vertical green area indicates the flare discussed in this paper. The blue dash-dot line shows the global trend of the stellar rotational modulation fitted with a trigonometric function. (b) Detrended white-light light curve of EV Lac around the flare discussed in this paper after subtracting of the rotational modulation.

$$L_{\text{peak}}^{\text{UVW2}}/L_{\text{peak}}^{\text{TESS}} \sim 0.49 \quad (21)$$

is obtained. Assuming the flare spectrum to be blackbody, this result may suggest that the temperature of it is low ($< 9000 \text{ K}$). On the other hand, the obtained flux ratio can be also explained by the Balmer and Paschen continuum flux ratio of optically thin radiation with a relatively low nonthermal electron beam of less than $5 \times 10^{11} \text{ erg cm}^{-2} \text{ s}^{-1}$ (see Figure 14 and Table 6 in Brasseur et al. 2023). The relationship between this value and spectral models will be discussed in detail in our future work.

In these days, some studies have estimated the UV flux from optical flare data because it is important in terms of its effect on exoplanets (Feinstein et al. 2020; Howard et al. 2020). On the other hand, there are studies that point to the discrepancy between such estimates and observed flux (Kowalski et al. 2019; Brasseur et al. 2023). The fact that NUV has the clear peak before the white-light peak, as found in this study, also warns against simple estimation of UV flux from optical continuum data. We need to more simultaneous UV and white-light samples to establish the picture of the relationship between UV and white-light flares.

4.4 Energy Distribution

We calculated radiated energy at each band and kinetic energy of the erupted prominence to investigate the energy distribution of this flare. We present quiescent-subtracted

Table 4. Peak luminosity and duration of the flare at each wavelength

	X-ray 0.5 – 4 keV	NUV 1600 – 3500 Å	White Light 6000 – 10000 Å	H α 6562.8 Å
Peak luminosity (10^{29} erg s $^{-1}$)	$1.9^{+0.2}_{-0.1}$	$0.33_{\pm 0.02}$ *	$0.67_{\pm 0.1}$ * / $4.2_{\pm 0.1}$ †	$0.07_{\pm 0.001}$
Rising time (min)	–	$1.7_{\pm 0.1}$ *	$7.0_{\pm 0.1}$	$7.4_{\pm 1.9}$
e-Folding time (min)	$77_{\pm 9.6}$	–	$19_{\pm 1.2}$	$61_{\pm 7.6}$

*These values are at r1 peak.

†This value is at r2 peak.

Table 5. Energy of radiation at each wavelength and the mass ejection

Radiation					Mass Ejection
X-ray 0.5 – 4 keV (erg)	NUV 1600 – 3500 Å (erg)	White Light Bolometric (erg)	H α 6000–10000 Å (erg)	H α 6562.8 Å (erg)	Kinetic Energy (erg)
$9.2^{+2.3}_{-1.6} \times 10^{32}$	$(0.2 - 4.0) \times 10^{31}$	$3.4_{\pm 1.1} \times 10^{32}$	$2.4_{\pm 1.2} \times 10^{32}$	$2.7_{\pm 0.4} \times 10^{31}$	$(0.02 - 15) \times 10^{31}$

light curves as in Figure 8a and calculated radiated energy at each band and the kinetic energy of the erupted prominence in the following manner:

X-ray: We calculated X-ray fluxes at each phase from the fitting (Figure 5) using the `flux` command in `xspec`. Then, we converted fluxes to luminosity using the distance of 5.05 pc (Gaia Collaboration et al. 2018). We subtracted the luminosity of Phase 0 as quiescence and created the quiescent-subtracted light curve as shown in Figure 8a. We assumed that the peak and start of the X-ray and H α flare are coincident (e.g., Kane 1974) and fitted the decay phase with the exponential function. When we fitted the X-ray light curve during the decay phase, we also assumed that the relationship between e -folding time of the X-ray ($\tau_{\text{decay}}^{\text{X-ray}}$) and H α ($\tau_{\text{decay}}^{\text{H}\alpha}$):

$$\log \tau_{\text{decay}}^{\text{X-ray}} = \log \tau_{\text{decay}}^{\text{H}\alpha} + 0.1 \pm 0.6, \quad (22)$$

which is empirically obtained in Kawai et al. (2022). Finally, we calculated radiated energy:

$$\begin{aligned}
E &= \int_{\text{rise}} L_{\text{flare}}(t) dt + \int_{\text{decay}} L_{\text{flare}}(t) dt \\
&\sim \int_{\text{rise}} (L_{\text{peak}} t / \tau_{\text{rise}}) dt \\
&+ \int_{\text{decay}} L_{\text{peak}} \exp\{-(t - \tau_{\text{rise}}) / \tau_{\text{decay}}\} dt \\
&\sim [(L_{\text{peak}} \times \tau_{\text{rise}}) / 2] + [L_{\text{peak}} \times \tau_{\text{decay}}], \quad (23)
\end{aligned}$$

where L_{peak} is the peak luminosity, τ_{rise} is the time between the start and the peak of the flare, and τ_{decay} is the e -folding time of the decay phase. The 0.5–4 keV X-ray peak luminosity and radiated energy are derived to be 1.9×10^{29} erg s $^{-1}$ & 9.2×10^{32} erg, respectively (Table 4 and 5).

H α : We calculated the quiescent-subtracted equivalent

widths of each time by integrating the symmetric components of H α (c.f. Figure 3b). After that, we converted the equivalent widths of each time to luminosity using Equation (1). We subtracted the average luminosity during two frames (at $-6 \sim 0$ min in Figure 8) before the start of H α flare as quiescence. Then, we created the quiescent-subtracted light curve (Figure 8 a2) and calculated the radiated energy using Equation (23). The H α peak luminosity and radiated energy are derived to be 7×10^{27} erg s $^{-1}$ and 2.7×10^{31} erg, respectively (Table 4 & 5). Note that the radiated energy of the blue-shifted excess component is not included in this energy.

NUV: We calculated the flare luminosity of each time from the light curve file created by `uvotevt1c` as discussed in Section 4.3. We subtracted the median luminosity as quiescence of 20 minutes before the start of the NUV flare. Since we only observed the rising phase in NUV as shown in Figure 8b, we calculated the lower limit of the radiation energy by integrating the observed light curve. We also assumed that e -folding time of NUV is shorter than that of white-light (e.g., Paudel et al. 2021; Brasseur et al. 2023; Tristan et al. 2023) and calculated the upper limit of the radiated energy using e -folding time of white-light flare and Equation (23). The NUV peak luminosity and radiated energy are derived to be 3.3×10^{28} erg s $^{-1}$ and $(0.2 - 4.0) \times 10^{31}$ erg, respectively (Table 4 & 5).

White light: We calculated the white-light bolometric energy of the flare from the white-light light curve using the method introduced by Shibayama et al. (2013). First, we divided the white-light light curve into the global trend and the flare component as shown in Figure 9a. We then took the difference between them and created the detrended light curve (Figure 9b). We took the flux of the

detrended curve as the ratio of the luminosity of flare luminosity to that of the star ($C'_{\text{flare}}(t)$) and estimated the flare area ($A_{\text{flare}}(t)$) as shown in the Equation (5) of Shibayama et al. (2013),

$$A_{\text{flare}}(t) = \frac{\pi R^2 C'_{\text{flare}}(t) \int R_{\lambda} B_{\lambda}(T_{\text{eff}}) d\lambda}{\int R_{\lambda} B_{\lambda}(T_{\text{flare}}) d\lambda} \quad (24)$$

where λ is the wavelength, B_{λ} is the Planck function, R_{λ} is the TESS response function (Ricker et al. 2015), T_{eff} is the effective temperature of the star (3270 K; Paudel et al. 2021), T_{flare} is a flare temperature of 10000 K (Mochnacki & Zirin 1980; Hawley & Fisher 1992), and R is the radius of the star ($0.35R_{\odot}$; Paudel et al. 2021). Assuming that flare radiation is a blackbody with a temperature of $T_{\text{flare}} = 10000$ K, flare luminosity L_{flare} is

$$L_{\text{flare}}(t) = \sigma_{\text{SB}} T_{\text{flare}}^4 A_{\text{flare}}(t) \quad (25)$$

where σ_{SB} is the Stefan-Boltzmann constant. Finally, we obtained the white-light bolometric flare energy by integrating $L_{\text{flare}}(t)$ over the duration of the white-light flare (the green-shaded period in Figure 9). The white-light bolometric energy is derived to be 3.4×10^{32} erg (Table 5).

We also calculated TESS band white-light energy by using equation (19):

$$\begin{aligned} E_{\text{WLF}}^{\text{TESS}} &= \int L_{\text{quiescence}}^{\text{TESS}} \times \Delta f^{\text{TESS}}(t) dt \\ &= 2.4 \times 10^{32} \text{ erg.} \end{aligned} \quad (26)$$

Kinetic Energy: We calculated the range of the kinetic energy ($Mv_{\text{blue}}^2/2$) of the erupted prominence using the mass range in Equation (16) and the peak velocity (v_{blue}) shown in Figure 6f. The kinetic energy range is $(0.02 - 15) \times 10^{31}$ erg (Table 5).

All parameters for the flare and the prominence are listed in Tables 4 and 5. According to Ikuta et al. (2023), a white-light flare of this magnitude occurs once every ~ 120 ks on EV Lac. X-ray and white-light radiated energy have the same order of magnitudes and they are one order higher than NUV and H α radiation. Though there is the large uncertainties in the kinetic energy, it roughly corresponds to the value expected from the flare-kinetic energy scaling law (Takahashi et al. 2016; Inoue et al. 2023).

Some previous studies have investigated the flare energy in X-ray and white light simultaneously (Emslie et al. 2012; Osten & Wolk 2015; Guarcello et al. 2019; Kuznetsov et al. 2021; Paudel et al. 2021; Stelzer et al. 2022; Namekata et al. 2023). Namekata et al. (2023) summarized the data and showed that there is several orders of magnitude variance in the distribution of the ratio of X-ray to white-light flare energy. Our obtained value ($E_{\text{WLF, bol}}/E_{\text{X}} \sim 0.4$) is in the variance. As solar studies also show that there is about an order of magnitude dispersion in flare energy distribution

(Emslie et al. 2012; Aschwanden et al. 2017), our result suggests the diversity of stellar flare energy distribution.

5 Summary and Conclusion

We observed EV Lac on 2022 October 24–27, and reported the first multiwavelength (X-ray, NUV, white light, and H α) detection of a stellar flare accompanied by H α blue-shifts, starting at 12:28 on October 25. The multiwavelength observed flare is a good sample for studying the whole picture of a flare accompanied by a mass ejection. The observed flare shows the following characteristics:

1. The radiation energies are 9.2×10^{32} erg (X-ray), $(0.2 - 4.0) \times 10^{31}$ erg (NUV), 3.4×10^{32} erg (White-light), and 2.7×10^{31} erg (H α).
2. One hour after the flare peak, a blue-shifted excess component of H α appeared, with its Doppler velocity at $\sim 100 \text{ km s}^{-1}$
3. When assuming that the observed blue-shifted excess component is attributed to a prominence eruption, the mass and kinetic energy of the prominence are estimated to

$$1 \times 10^{15} \text{ g} < M < 1 \times 10^{18} \text{ g} \quad (27)$$

$$2 \times 10^{29} \text{ erg} < E_{\text{kin}} < 2 \times 10^{32} \text{ erg}, \quad (28)$$
 respectively. This follows the energy-mass scaling law of solar and stellar flares (Takahashi et al. 2016; Inoue et al. 2023; Notsu et al. 2023).
4. The rising phase of the white-light flare has a substructure consisting of a gradual rise and a rapid rise. Even during the gradual rise of white-light, NUV emission has already increased rapidly. The ratio of flux in NUV to white light at the peak during the gradual phase was ~ 0.49 .

During this campaign observation, we have also performed coordinated observations with Five-hundred-meter Aperture Spherical radio Telescope (FAST; Nan 2006; Nan et al. 2011; Zhang et al. 2023) and 85 cm telescope at Xinglong Station of National Astronomical Observatories, Chinese Academy of Sciences. We will further discuss the flare radiation mechanism by combining radio and multi-band optical photometric data in our upcoming papers.

Acknowledgments

The NICER and Swift data used in this study were obtained through ToO program ID: 43723 (NICER) and ID: 17657 (Swift), respectively. This paper includes data collected with the TESS mission, obtained from the MAST data archive at the Space Telescope Science Institute (STScI). Funding for the TESS mission is provided by the NASA Explorer Program. STScI is operated by the Association of

Universities for Research in Astronomy, Inc., under NASA contract NAS 5-26555. The optical spectroscopic data used in this study were obtained through 2022B open-use program with the 2m Nayuta telescope, which is located at Nishi-Harima Astronomical Observatory, Center for Astronomy, University of Hyogo. We thank Megumi Shidatsu (Ehime University) for her useful comments and discussions on the UVOT data analysis. We thank Swift helpdesk for the suggestion on the UVOT data analysis. We thank Isaiah Tristan and Adam Kowalski (University of Colorado Boulder) for providing their modeling data. We thank Hui Tian (Peking University) for his helpful comments and suggestions. This work is supported by JSPS KAKENHI Grant Numbers 21J00316 (K.N.), 20K04032, 20H05643 (H.M.), 21J00106 (Y.N.), 21H01131 (H.M., D.N., S.H., K.S.), 21H04493 (T.G.T.) and RIKEN Hakubi project (PI: Teruaki Enoto). Y.N. acknowledge support from NASA ADAP award program Number 80NSSC21K0632 (PI: Adam Kowalski).

Appendix. X-ray spectral fitting with the fixed quiescent component

We also conducted X-ray spectral fitting with the fixed quiescent component during the flare. This fitting method assumes that there is no significant variation in the quiescent component during the flare (e.g., Hamaguchi et al. 2023).

Based on the results of the spectral analysis of quiescent spectra (c.g. Figure 5 e and f), we analyzed the spectra for each phase after the flare occurred (Phase 1-5). For the analysis of flare spectra, we fixed the best fit values of October 26 NICER spectrum as the quiescent component. Then, we fit the flare component with two temperature collisionally-ionized models (*vap*ec). We linked abundance between flare components. For Phase 3 spectrum obtained by Swift XRT, we fixed abundance to the best-fit value of Phase 2, which is the closet phase to Phase 3, since it cannot be well determined due to a lack of statistics. As in the analysis of quiescent spectra, we tried to fit flare spectra with the model that multiplies the sum of the quiescent and flare components by an interstellar absorption fixed to the literature value ($N_{\text{H}} = 4.0 \times 10^{18} \text{ cm}^{-2}$; Paudel et al. 2021). However, spectra of Phase 2, 3, and 4 were not acceptably explained by this model. Specifically, the temperature of the flare component became overwhelmingly higher (3 – 70 keV / 35 – 810 MK) than Phase 1, which is closer to the peak of the flare, to fit the low energy side (< 1 keV) of Phase 2-4 spectra. These fitting parameters are physically unacceptable because the loop plasma should be cooled via radiation after the peak of the flare (Shibata & Magara 2011). As mentioned in Section 3.1, some small flares occurred before and after Phase 3 and 4. Therefore, we tried to fit the flare component of Phase 3 and 4 by adding an extra *vap*ec components with a fixed

interstellar absorption. However, the spectra could not be fitted well no matter how many components were added.

Then, to improve the fits, we set N_{H} free for Phase 2, 3, and 4. We unified the number of flare *vap*ec components to two for all flare spectra. When we set N_{H} free, spectra of Phase 2, 3, and 4 could be well fitted. These flare spectra and the results of the spectral fit are shown in Figure 10 a-d, and g. Table 6 lists the best-fit parameters for these fitting. As shown in Table 6, best-fit values of hydrogen column density increased by two orders of magnitude from $4 \times 10^{18} \text{ cm}^{-2}$ to $3.5 - 9.3 \times 10^{21} \text{ cm}^{-2}$ during Phase 2-4.

Moschou et al. (2017) suggested that CMEs passing through the line-of sight direction cause increase of hydrogen column density. In this flare, the ejected plasma, seen as the blueshift of $\text{H}\alpha$, may also have caused X-ray absorption. When the prominence is optically thick, from Equations (7), (8), and (13), hydrogen column density of the prominence $N_{\text{H}}^{\text{P}} = n_{\text{H}}D$ is

$$7 \times 10^{19} \text{ cm}^{-2} < N_{\text{H}}^{\text{P}} < 6 \times 10^{21} \text{ cm}^{-2}. \quad (\text{A1})$$

This value is consistent with the observed hydrogen column density during Phase 2-4 shown in Table 6.

However, the fitting parameters of low temperature components during Phase 2-4 (0.10 keV / 0.14 keV / 0.09 keV) are lower than the lowest component of the quiescence (0.24 keV). This means that a part of the flare loop is much cooler than the coronal plasma in the quiescent phase. As such situation is not natural, we hesitate to declare the increase of hydrogen column density and adopted the fitting without the fixed quiescent component as described in Section 3.2.2.

References

- Airapetian, V. S., Glocer, A., Gronoff, G., et al. 2016, *Nat. Geosci.*, 9, 452
- Airapetian, V. S., Barnes, R., Cohen, O., et al. 2020, *IJAsB*, 19, 136
- Aizawa, M., Kawana, K., Kashiyama, K., et al. 2022, *PASJ*, 74, 1069.
- Arnaud, K. A. 1996, in *ASP Conf. Ser. 101, XSPEC: The First Ten Years*, ed. G. H. Jacoby & J. Barnes (San Francisco, CA: ASP), 17
- Aschwanden, M. J., Caspi, A., Cohen, C. M. S., et al. 2017, *ApJ*, 836, 17. doi:10.3847/1538-4357/836/1/17
- Brasseur, C. E., Osten, R. A., Tristan, I. I., & Kowalski, A. F. 2023, *ApJ*, 944, 5
- Burrows, D. N., Hill, J. E., Nousek, J. A., et al. 2005, *SSRv*, 120, 165
- Chen, H., Tian, H., Li, H., et al. 2022, *ApJ*, 933, 92.
- Emslie, A. G., Dennis, B. R., Shih, A. Y., et al. 2012, *ApJ*, 759, 71.
- Favata, F., Reale, F., Micela, G., et al. 2000, *A&A*, 353, 987

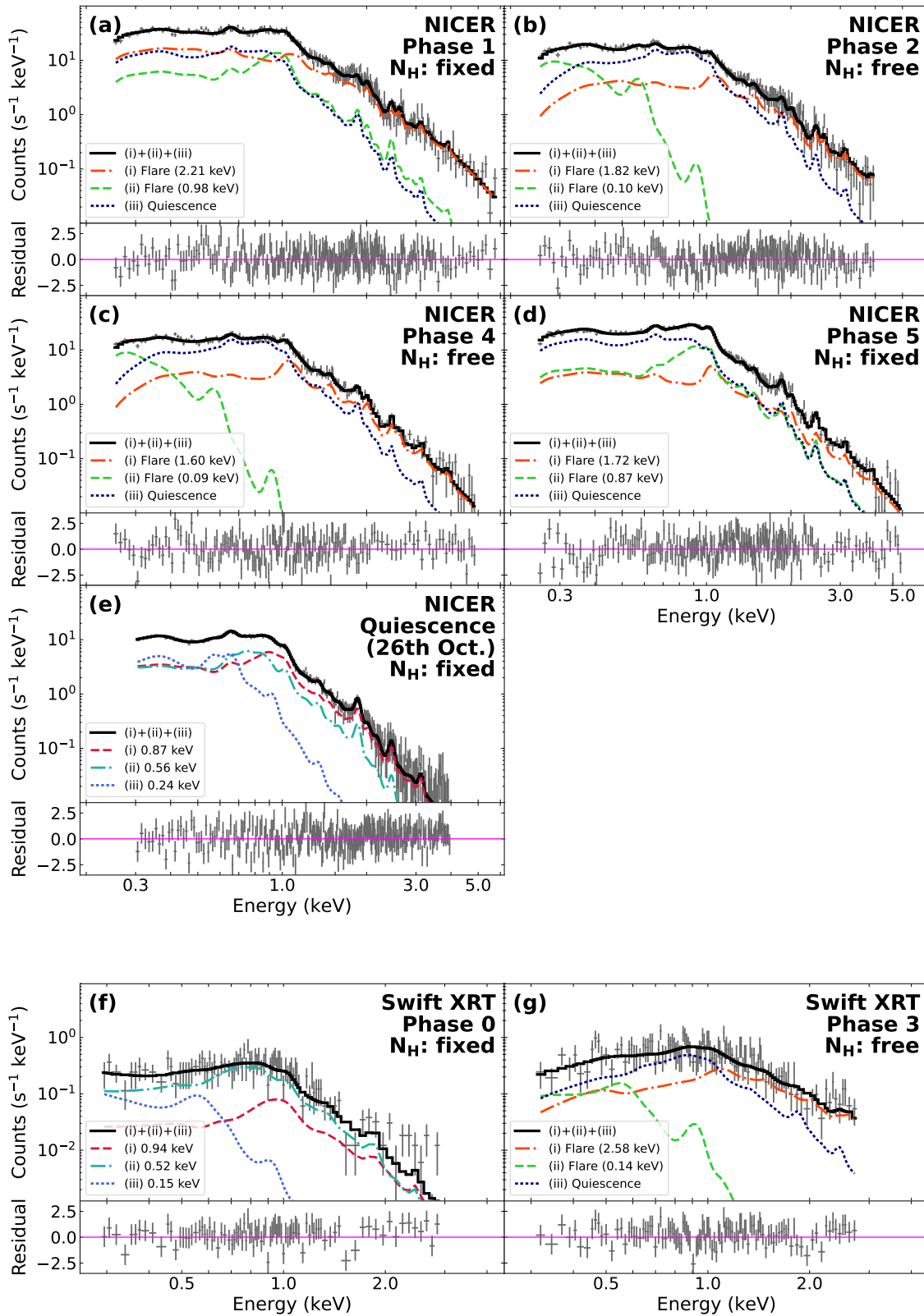


Fig. 10. X-ray spectra at each phase shown in Figure 2. Panels (a), (b), (c), (d) and (g): Spectra during the flare. The best-fit curves for the quiescence spectrum + two-component νapec models are shown by solid black lines for flare spectra. Navy dotted lines, orange dashdot lines, and lime dashed lines represent the quiescence spectrum, the high temperature component, and the low temperature component, respectively. Panels (e) and (f): Spectra during the quiescence. The best-fit curves for the three-component νapec models are shown by solid black lines for quiescence spectra. Red dashed lines, sea green dashdot lines, and cornflower blue lines represent the high temperature component, the medium temperature component, and the low temperature component, respectively.

Table 6. Best-fit parameters of spectra during the flare*

	NICER				Swift XRT	
	Phase 1	Phase 2	Phase 4	Phase 5	Phase 3	
Exposure (ks)	0.42	0.71	0.71	1.19	0.82	
tbabs						
N_{H} (10^{18} cm $^{-2}$)	4.00	$348_{\pm 46.3}$	$354_{\pm 42.2}$	4.00	$925_{\pm 334}$	
vaptec (High Temp.)						
Temperature	kT (keV)	$2.21_{\pm 0.13}$	$1.82_{\pm 0.14}$	$1.60_{\pm 0.07}$	$1.72_{\pm 0.11}$	$2.58_{\pm 0.91}$
	T (MK)	$25.7_{\pm 1.51}$	$21.1_{\pm 1.63}$	$18.6_{\pm 0.81}$	$20.0_{\pm 1.28}$	$29.9_{\pm 10.6}$
norm (10^{-2})	$2.09_{\pm 0.12}$	$0.68_{\pm 0.46}$	$0.64_{\pm 0.04}$	$0.42_{\pm 0.04}$	$1.03_{\pm 0.12}$	
vaptec (Low Temp.)						
Temperature	kT (keV)	$0.98_{\pm 0.04}$	$0.10_{\pm 0.01}$	$0.09_{\pm 0.01}$	$0.87_{\pm 0.03}$	$0.14_{\pm 0.06}$
	T (MK)	$11.37_{\pm 0.46}$	$1.16_{\pm 0.12}$	$1.05_{\pm 0.12}$	$10.11_{\pm 0.35}$	$1.63_{\pm 0.70}$
norm (10^{-2})	$0.61_{\pm 0.11}$	$1.35_{\pm 0.42}$	$1.82_{\pm 0.83}$	$0.40_{\pm 0.04}$	$1.06_{\pm 1.36}$	
Z (Z_{\odot})	He	1.00	1.00	1.00	1.00	1.00
	C	$0.74_{\pm 0.18}$	$0.29_{\pm 0.09}$	$0.17_{\pm 0.06}$	$0.56_{\pm 0.14}$	0.29
	N	$0.74_{\pm 0.18}$	$0.29_{\pm 0.09}$	$0.17_{\pm 0.06}$	$0.56_{\pm 0.14}$	0.29
	O	$0.74_{\pm 0.18}$	$0.29_{\pm 0.09}$	$0.17_{\pm 0.06}$	$0.56_{\pm 0.14}$	0.29
	Ne	1.00	1.00	1.00	$3.16_{\pm 0.42}$	1.00
	Mg	$0.43_{\pm 0.20}$	1.00	1.00	1.00	1.00
	Al	1.00	1.00	1.00	1.00	1.00
	Si	$0.65_{\pm 0.14}$	$0.49_{\pm 0.23}$	$0.79_{\pm 0.21}$	$0.68_{\pm 0.11}$	0.49
	S	1.00	1.00	1.00	1.00	1.00
	Ar	1.00	1.00	1.00	1.00	1.00
	Ca	1.00	1.00	1.00	1.00	1.00
	Fe	$0.30_{\pm 0.04}$	$0.30_{\pm 0.10}$	$0.32_{\pm 0.08}$	$0.29_{\pm 0.03}$	0.30
	Ni	1.00	1.00	1.00	1.00	1.00
	χ^2 (<i>d.o.f</i>)	268 (250)	215 (219)	211 (160)	252 (203)	86 (106)

* The error ranges correspond to 90% confidence level. Values without errors mean that they are fixed.

- Feinstein, A. D., Montet, B. T., Ansdell, M., et al. 2020, *AJ*, 160, 219.
- Gaia Collaboration, Brown, A. G. A., Vallenari, A., et al. 2018, *A&A*, 616, A1
- Gendreau, K. C., Arzoumanian, Z., Adkins, P. W., et al. 2016, *SPIE Proc.*, 99051H
- Guarcello, M. G., Micela, G., Sciortino, S., et al. 2019, *A&A*, 622, A210
- Hamaguchi, K., Reep, J. W., Airapetian, V., et al. 2023, *ApJ*, 944, 163
- Hawley, S. L., & Fisher, G. H. 1992, *ApJS*, 78, 565
- Heinzl, P., Gouttebroze, P., & Vial, J.-C. 1994, *A&A*, 292, 656
- Hirayama, T. 1986, in *Coronal and Prominence Plasmas*, Vol. 2442, ed. A. I. Poland (Washington, DC: NASA), 149
- Honda, S., Notsu, Y., Namekata, K., et al. 2018, *PASJ*, 70, 62
- Howard, W. S., Corbett, H., Law, N. M., et al. 2020, *ApJ*, 902, 115
- Howard, W. S., & MacGregor, M. A. 2022, *ApJ*, 926, 204
- Ikuta, K., Namekata, K., Notsu, Y., et al. 2023, *ApJ*, 948, 64
- Inoue, S., Maehara, H., Notsu, Y., et al. 2023, *ApJ*, 948, 9
- Jackman, J. A. G., Shkolnik, E., Million, C., et al. 2023, *MNRAS*, 519, 3564
- Kane, S. R. 1974, in *IAU Symp. 57, Coronal Disturbances*, ed. G. A. Newkirk (Dordrecht: D. Reidel Publishing), 105
- Kawai, H., Tsuboi, Y., Iwakiri, W. B., et al. 2022, *PASJ*, 74, 477
- Konings, T., Baeyens, R., & Decin, L. 2022, *A&A*, 667, A15
- Kowalski, A. F., Hawley, S. L., Wisniewski, J. P., et al. 2013, *ApJS*, 207, 15.
- Kowalski, A. F., Mathioudakis, M., Hawley, S. L., et al. 2016, *ApJ*, 820, 95.
- Kowalski, A. F., Wisniewski, J. P., Hawley, S. L., et al. 2019, *ApJ*, 871, 167.
- Kurokawa, H., Hanaoka, Y., Shibata, K., et al. 1987, *Sol. Phys.*, 108, 251.
- Kuznetsov, A. A., & Kolotkov, D. Y. 2021, *ApJ*, 912, 81
- Labrosse, N., Heinzl, P., Vial, J. C., et al. 2010, *SSRv*, 151, 243
- Leitzinger, M., Odert, P., & Heinzl, P. 2022, *MNRAS*, 513, 6058
- Leitzinger, M. & Odert, P. 2022, *Serbian Astronomical Journal*, 205, 1. doi:10.2298/SAJ2205001L

- Li, D., Li, C., Qiu, Y., et al. 2023, *ApJ*, 954, 7.
- Loyd, R. O. P., Mason, J. P., Jin, M., et al. 2022, *ApJ*, 936, 170
- Lu, H. peng., Tian, H., Zhang, L. yun ., et al. 2022, *A&A*, 663, A140.
- Maehara, H., Notsu, Y., Namekata, K., et al. 2021, *PASJ*, 73, 44
- Mason, E. I., Antiochos, S. K., & Vourlidas, A. 2021, *ApJL*, 914, L8.
- Mochnecki, S. W., & Zirin, H. 1980, *ApJ*, 239, L27
- Moschou, S. P., Drake, J. J., Cohen, O., Alvarado-Gomez, J. D., & Garraffo, C. 2017, *ApJ*, 850, 191
- Moschou, S. P., Drake, J. J., Cohen, O., et al. 2019, *ApJ*, 877, 105
- Mulkidjanian, A. Y., Cherepanov, D. A., & Galperin, M. Y. 2003, *BMC Evolutionary Biology*, 3, 12
- Muheki, P., Guenther, E. W., Mutabazi, T., et al. 2020, *MNRAS*, 499, 5047.
- Muheki, P., Guenther, E. W., Mutabazi, T., & Jurua, E. 2020, *A&A*, 637, A13
- Namekata, K., Sakaue, T., Watanabe, K., et al. 2017b, 1238 *ApJ*, 851, 91
- Namekata, K., Maehara, H., Sasaki, R., et al. 2020, *PASJ*, 72, 68.
- Namekata, K., Maehara, H., Honda, S., et al. 2022a, *NatAs*, 6, 241
- Namekata, K., Maehara, H., Honda, S., et al. 2022b, *arXiv:2211.05506*.
- Namekata, K., Airapetian, V. S., Petit, P., et al. *ApJ* in press (*arXiv:2311.07380*)
- Nan, R. 2006, *ScChG*, 49, 129
- Nan, R., Li, D., Jin, C., et al. 2011, *IJMPD*, 20, 989
- Neupert, W. M., 1968, *ApJL*, 153, L59.
- Notsu, Y., Kowalski, A. F., Maehara, H., et al. *ApJ* in press (*arXiv: 2310.02450*)
- Osten, R. A., Hawley, S. L., Allred, J., et al. 2006, *ApJ*, 647, 1349
- Osten, R. A., & Wolk, S. J. 2015, *ApJ*, 809, 79
- Otsu, T., Asai, A., Ichimoto, K., Ishii, T. T., & Namekata, K. 2022, *ApJ*, 939, 98
- Parenti, S. 2014, *LRSP*, 11, 1
- Paudel, R. R., Barclay, T., Schlieder, J. E. et al. 2021 *ApJ* 922 31
- Poole, T. S., Breeveld, A. A., Page, M. J., et al. 2008, *MNRAS*, 383, 627
- Reiners, A., Zechmeister, M., Caballero, J. A., et al. 2018, *A&A*, 612, A49.
- Remillard, R. A., Loewenstein, M., Steiner, J. F., et al 2022, *AJ*, 163, 130
- Ricker, G. R., Winn, J. N., Vanderspek, R., et al. 2015, *JATIS*, 1, 014003
- Segura, A. 2018, *Handbook of Exoplanets*, 73.
- Shibata, K. & Uchida, Y. 1986, *Sol. Phys.*, 103, 299.
- Shibata, K., & Yokoyama, T. 2002, *ApJ*, 577, 422
- Shibata, K., & Magara, T. 2011, *LRSP*, 8, 6
- Shibayama, T., Maehara, H., Notsu, S., et al. 2013, *ApJS*, 209, 5
- Sinha, S., Srivastava, N., & Nandy, D. 2019, *ApJ*, 880, 84
- Stelzer, B., Caramazza, M., Raetz, S., Argiroffi, C., & Coffaro, M. 2022, *A&A*, 667, L9,
- Tei, A., Sakaue, T., Okamoto, T., et al. 2018, *PASJ*, 70, 100
- Takahashi, T., Mizuno, Y., & Shibata, K. 2016, *ApJL*, 833, L8
- Tody, D., 1986, *Proc. SPIE*, 627, 733
- Tristan, I. I., Notsu, Y., Kowalski, A.F., et al. 2023, *ApJ*, 951, 33
- Veronig, A. M., Odert, P., Leitzinger, M., et al. 2021, *Nature Astronomy*, 5, 697
- Vida, K., Kriskovics, L., Oláh, K., et al. 2016, *A&A*, 590, A11
- Vida, K., Leitzinger, M., Kriskovics, L., et al. 2019, *A&A*, 623, A49
- Zhang, J., Tian, H., Zarka, P., et al. 2023, *ApJ*, 953, 65.
- Zirin, H. 1969, *Sol. Phys.*, 7, 243.